Dielectric function and electronic structure of non-degenerate rocksalt ScN: Spectroscopic ellipsometry and *GW*-calculations

Jona Grümbel,* Rüdiger Goldhahn, and Martin Feneberg
Institut für Physik, Otto-von-Guericke-Universität Magdeburg, Universitätsplatz 2, 39106, Magdeburg, Germany

Yuichi Oshima
Research Center for Electronic and Optical Materials, National Institute for Materials Science , 1-1 Namiki, Tsukuba, Ibaraki 305-0044, Japan

Hazem Abu-Farsakh
Department of Mathematics and Sciences, Prince Sultan University, Riyadh 11586, Saudi-Arabia

Abdallah Qteish
Department of Physics, Yarmouk University, Irbid 21163, Jordan

In this work we determine the dielectric function of ScN in a spectral range from 0.9 eV to 6.4 eV by spectroscopic ellipsometry from non-degenerately doped, bulk-like samples. Several models are applied to the obtained dielectric functions yielding main critical point transitions energies. These results are compared with state-of-the-art computations, where the band structure of ScN is calculated using Heyd-Scuseria-Ernzerhof (HSE06) hybrid functionals and quasi-particle corrections in the G_0W_0 approach. Furthermore, the dielectric function of ScN is derived from the computed band structure by solving the Bethe-Salpeter-equation to account for electron-hole-pair interactions. We find exceptional agreement between computed and experimentally determined dielectric functions, where discrete excitons are not observed experimentally. We extrapolate an intrinsic direct bandgap of (2.182±0.004)eV and an intrinsic indirect bandgap of (1.08±0.02eV) by taking into account many-body-effects, while higher energy critical point transition energies of Γ-point transitions are averaged over all samples, yielding $E_\Gamma = (3.853 \pm 0.006)$eV and $E_{\Gamma'} = (5.21 \pm 0.02)$eV. Critical point transitions in the computed band structure, though, deviate from the experimental ones due to the omission of electron-hole-interaction, where the deviation increases with increasing energy. The dielectric limit of the electronic system is determined as $\varepsilon_\infty = (8.38 \pm 0.04)$ from experiment, where the computed dielectric function reveals almost the same value ($\varepsilon_\infty = 8.33$). Along with other previous publications we conclude that solving the Bethe-Salpeter-equation is indispensable for the computation of the dielectric function of semiconductors even in the absence of discrete excitons.

I. INTRODUCTION

Although the vast majority of device applications consist of thin, strained, and doped films as active layers, there is a fundamental need to understand the bulk properties of a given material to control the desired properties of a thin film properly. This goal has not yet been achieved sufficiently on ScN for mainly two reasons: (i) there are only few bulk-like crystals available[1–6] and (ii) most of them still exhibit either carrier densities beyond the degeneracy limit[5, 6], high structural disorder[1, 4], or macroscopically rough surfaces[1, 4, 5]. The bandgap of a semiconductor is particularly sensitive to the free carrier concentration by means of bandgap-renormalization (BGR) and the absorption edge by means of band-filling, known as Burstein-Moss-shift (BMS). Corrections regarding the latter have been discussed only for degenerately doped ScN samples[7, 8], while the bandgap renormalization, to our knowledge, was not accounted for in ScN. Knowledge of the intrinsic indirect and direct bandgaps of ScN is desirable as it exhibits promising properties for several applications, e.g. as (transparent) conductive buffer layer for lattice matched GaN growth[9] or for thermoelectric conversion devices[10, 11], not speaking of the exploding research interest in the ternary ScAlN alloy system due to e.g. enhanced piezoelectricity[12] and ferroelectricity[13]. In this work, we conduct a precise evaluation of electronic transition energies in ScN in the spectral range from 0.9 eV-6.4 eV by employing spectroscopic ellipsometry on high quality bulk-like and non-degenerately doped ScN films. For the determination of direct bandgaps we use methods beyond the widely misused Tauc-plot method, whose applicability on the optical response of semiconductors underlies several limitations[14]. The experimental results are backed up by state-of-the-art calculations: a quasiparticle G_0W_0 approach for the electronic structure, and by solving the Bethe-Salpeter equation, starting from the G_0W_0 results, for the dielectric function. The latter approach takes into account the electron-hole interactions in the optical response.

II. METHODS AND SAMPLES

A. Computation

The first-principles calculations were performed employing the projector-augmented-wave (PAW) method as implemented in the Vienna *Ab initio* Simulation Package (VASP) [15–17]. Soft PAW pseudopotentials were used to represent the electron-ion interactions, in which the 3*s*, 3*p*, and 3*d* states of Sc and the 2*s* and 2*p* states of N are explicitly treated as valence states. The adopted pseudopotentials are optimized for accurately describing unoccupied states far above the Fermi level. The quasiparticle (QP)

* jona.gruembel@ovgu.de

Table I: List of substrate and ScN layer orientation, ScN film thickness, selected ellipsometry layer model parameters (bold), x-ray rocking curve full width at half maximum (XRC-FWHMs), and free carrier concentration determined from Hall measurements. The roughness displays the thickness of the Bruggeman EMA layer (1:1 layer/void ratio). The XRC twist FWHMs correspond to (200) and (220) reflections and the XRC tilt FWHMs correspond to (131) and ($\bar{2}$40) reflections for m- and r-sapphire substrates, respectively

	substrate	ScN layer orientation	thickness	**thickness non-uniformity**	**roughness**	**point-by-point fit cutoff**	XRC FWHM twist	XRC FWHM tilt	strain out-of-plane	n_{Hall}
			(µm)	(%)	(nm)	eV	(°)	(°)	(10^{-4})	(10^{18} cm^{-3})
A_1	r-sapphire	(100)	38.4	**2.2**	**4.1**	**1.44**	0.07	0.34	-2.9	7.7
B_1			19.2	**2.0**	**5.1**	**1.55**	0.09	0.45	-0.22	1.3
C_1			9.6	**3.9**	**4.4**	**1.8**	0.12	0.55	-2.4	15
D			**1.36**	**0**	**4.1**	**0.93**	0.28	0.80	-2.9	27
A_2	m-sapphire	(110)	44.8	**0**	**5.3**	**1.44**	0.03	0.05	-0.95	1.5
B_2			22.4	**0**	**6.9**	**1.67**	0.04	0.08	-1.6	3.2
C_2			11.2	**0**	**7.1**	**1.8**	0.05	0.14	-1.6	5.2
E			3.7	**0**	**7.5**	**1.94**	0.09	0.35	3.1	12

electronic band structure was obtained employing a single-shot *GW* approach starting from HSE06 hybrid functional [18, 19] data (hereafter denoted as HSE06-G_0W_0). The HSE06 calculations, in turn, were performed starting from DFT wavefunctions, employing the generalized gradient exchange-correlation functional of Perdew, Burke, and Ernzerhof (GGA-PBE) [20]. The electronic wavefunctions were expanded in a plane-wave basis set with a cutoff energy of 350 eV, and the Brillouin zone was sampled using a regular $20 \times 20 \times 20$ Monkhorst-Pack k-mesh [21]. A total of 256 bands were used to obtain the QP energies. Convergence with respect to the plane-wave cutoff energy, k-point sampling, and number of bands was carefully verified. The QP band structure along the high-symmetry directions was interpolated using maximally-localized Wannier functions (MLWFs) [22]. The HSE06-G_0W_0 approach provides a reliable description of the underlying electronic structure for the calculation of the dielectric function [23–25].

The frequency-dependent dielectric function was then calculated by solving the Bethe-Salpeter equation (BSE), which accounts for the excitonic and local-field effects (LFEs) [26]. To obtain the dielectric function over a wide spectral range (up to 60 eV) at affordable computational cost, we adopted a multi-grid strategy similar to that used by Schleife *et al.* [24]. In our approach, the Brillouin zone was sampled with successively coarser k-point meshes for progressively wider photon-energy regions. An adequate number of conduction bands (CBs) was used for each case. As the k-point sampling was reduced, the number of CBs was increased, and convergence with respect to the included CBs was verified. We used regular $20\times20\times20$, $16\times16\times16$, $12\times12\times12$, and $8\times8\times8$ Γ-centered k-meshes for transitions up to 12.3 eV, 21.7 eV, 38.0 eV, and 60.0 eV, respectively. The resulting imaginary parts of the dielectric function ε_2 were found to merge smoothly at 8.3 eV, 20.7 eV, and 36.3 eV. The real part ε_1 was then calculated using the Kramers-Kronig relation. A Lorentzian broadening of 0.15 eV was used for the first two meshes and 0.20 eV for the coarser meshes. As high-energy transitions are explicitly included in our multi-grid BSE scheme, the obtained dielectric constant (ε_∞) does not require a rigid shift of ε_1. For comparison, the dielectric function was also calculated using the independent-particle approximation (IPA) starting from the HSE06-G_0W_0 electronic structure, with a regular $20\times20\times20$ Γ-centered k-mesh across the whole spectrum up to 60 eV.

B. Spectroscopic ellipsometry and transmission

Spectroscopic ellipsometry is capable of determining both real and imaginary parts of the dielectric function by measuring the angle Ψ and retardance Δ of polarization upon reflection of polarized light. For an isotropic sample, the measured quantities Ψ and Δ are linked to the so-called pseudo dielectric function by

$$\langle\varepsilon\rangle = \sin^2\Phi\left[1+\tan^2\Phi\left(\frac{1-\rho}{1+\rho}\right)^2\right] \tag{1}$$

where Φ is the angle of incidence (AOI) and ρ is the ratio of the diagonal Fresnel coefficients r_{pp} and r_{ss}:

$$\rho = \frac{r_{\mathrm{pp}}}{r_{\mathrm{ss}}} = \tan\Psi e^{\mathrm{i}\Delta} \tag{2}$$

We use a Woollam VASE rotating compensator laboratory ellipsometer for up to 6.4 eV photon energy, where the spectral resolution is set to 4 meV, 12 meV, and 23 meV at 2.2 eV, 3.8 eV, and 5.2 eV by keeping the grating monochromator slit width constant at 400 nm, respectively. We acquire data with an energy step width of 5 meV at 45°, 60°, and 75° AOI. Data acquisition and analysis is done by the Woollam WVASE32 software. To obtain the dielectric function of the material, a layer model is applied, consisting of an anisotropic sapphire substrate model and a ScN layer with a Bruggeman effective medium approximation (EMA)[27] roughness layer on top, where we use a 1:1 layer/void ratio. Additionally, for samples A_1, B_1, and C_1, we account for a non-ideal model by means of thickness non-uniformity as displayed in Tab. I. The thickness of the ScN layer is fixed to the values obtained from initial SEM measurements, only for sample D it is a free parameter within the layer model (see Tab. I). As discussed below, the surface of (110) layers is quite different to that of (100)

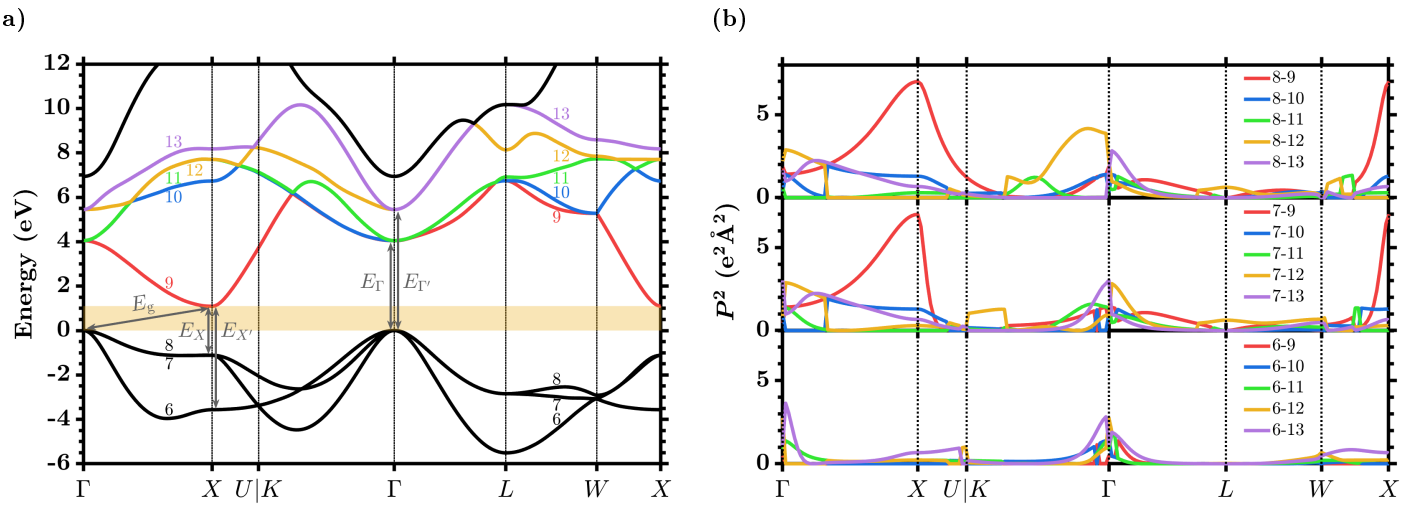

Figure 1: (a) Quasi-particle band structure of ScN and (b) squared transition dipole moment for optical transitions from the three uppermost valence bands (6-8) to the five lowest conduction bands (9-13) along high symmetry directions.

layers, where the former exhibit a higher surface roughness. Because an AOI of 75° is particularly surface sensitive, we were not able to model the data of (110) ScN layers when 75° AOI is included. Consequently, we exclude this AOI from our analysis for those samples. The dielectric function of the ScN layer then is obtained by a point-by-point fit of its optical constants.

Normal incidence transmission is recorded by a Shimadzu spectrophotometer (UV-3101PC + MPC-3100 UV-VIS-NIR) in the spectral range from 830 nm to 1800 nm (0.69 eV to 1.49 eV), where a wave length step width of 1 nm was used, which corresponds to a energy step width of 1 meV at 1.1 eV photon energy, similar to the selected spectral resolution.

C. Samples

Samples were grown by halide-vapor-phase epitaxy (HVPE) either on r- or m-plane sapphire substrates, using $ScCl_3$ and NH_3 gases in a reactor with specific parameters to avoid oxygen incorporation, yielding single crystalline ScN layers as reported in ref. [3]. Sample parameters are listed in Tab. I, where shared letters (e.g. A_1 and A_2) denote same-run samples. Among others, the samples were initially characterized by x-ray diffraction (XRD), Hall measurements, and scanning electron microscopy (SEM), which reveals smooth surfaces for (100) ScN films but less smooth surfaces for (110) ScN films. The surfaces of (100) ScN films exhibit large plateaus while the (110) films show a hill-valley-type structure[3]. From XRD rocking curves (XRCs), full widths of half maxima (FWHMs) between 0.03° and 0.28° are obtained from the symmetric (200) and (220) reflexes for (100) and (110) ScN layers, respectively, indicating excellent structural quality for all 8 samples. They exhibit thicknesses from 1.3 µm to 45 µm and free carrier densities between 1.3×10^{18} cm^{-3} and 2.7×10^{19} cm^{-3} (see Tab. I). The degeneracy limit in ScN is reported to be around 3×10^{19} cm^{-3} [28, 29], hence all samples have free carrier concentrations below or near the degeneracy point. Taking into account the literature value for strain free ScN ($a_0 = 4.5047$ Å[30]) the strain in our samples is $|\epsilon| < 4\times10^{-4}$ (see Tab. I), which is negligible in the context of our study. For our analysis we conduct new Hall measurements in van-der-Pauw geometry (see Tab. I) to ensure that we use the correct free carrier concentrations, which may have changed due to aging processes. Nevertheless, we expect the aging, particularly a possible oxidation, to be weak due to the high structural quality of both the bulk and the sample surfaces. Samples were cleaned ultrasonically in ethanol or acetone to remove possible surface contaminants prior to ellipsometry measurements. Results on sample A_1 are already published[31], but the cleaning procedure and slightly different measurement settings reveal changes in the optical constants, which are discussed below.

III. RESULTS

A. Band structure

The band structure of ScN was determined in numerous works before[8, 28, 32–43], where only refs. [8, 35, 36, 42, 43] use the full quasi-particle approach. Qualitatively, though, they all agree that ScN is an indirect band gap semiconductor with its band gap located between the Γ-point valence band maximum (VBM) and the X-point conduction band minimum (CBM), while the lowest direct gap occurs at the X-point. The present calculation shows the same behavior as displayed in Fig. 1a. The optical response, i.e. the dielectric function, is particularly sensitive to critical points in the band structure, which are characterized by $|\nabla_{\boldsymbol{k}} E_{\mathrm{CV}}| = 0$. In the absence of discrete exciton states (see Sec. III C), we assume the qualitative band shape around each critical point to be preserved upon electron-hole-interaction renormalization. Four critical point transitions, labeled X, Γ, X', and Γ', are of interest in this work as they appear at energies below 6.4 eV. The present band structure calculation yields transi-

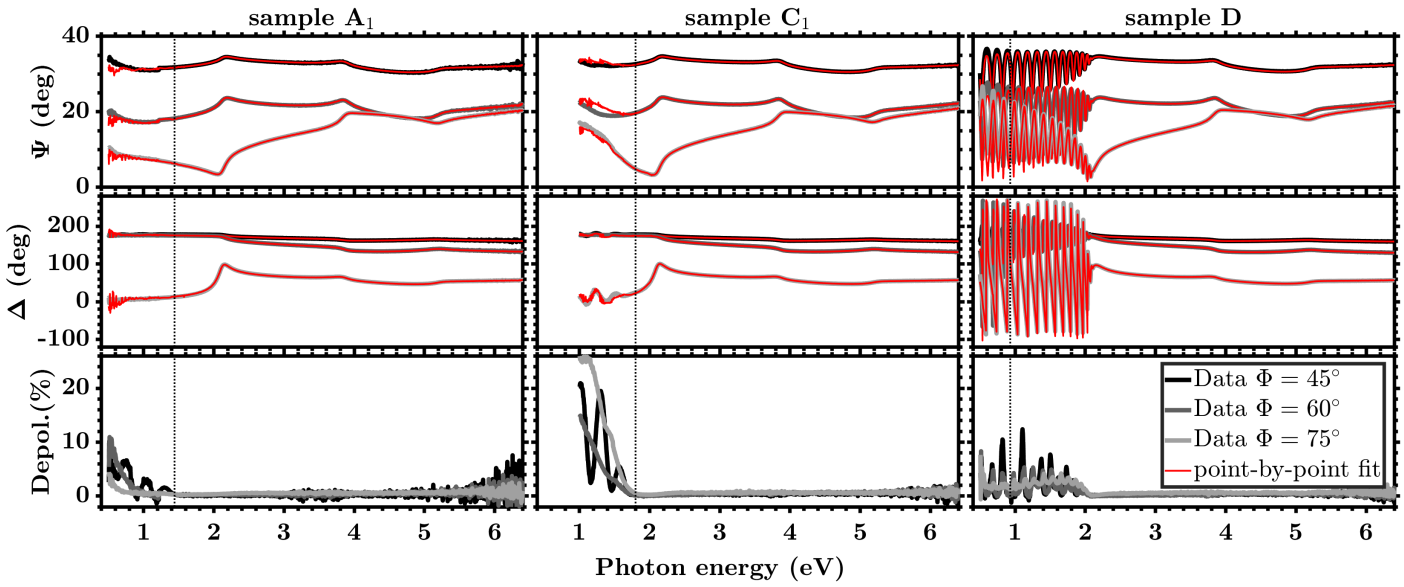

Figure 2: Measured ellipsometric parameters Ψ (upper panel) and Δ (middle panel) for incidence angles of 45° (black lines), 60° (dark gray lines), and 75° (light gray lines) with corresponding point-by-point fit results (red lines) for samples A_1, C_1, and D. The lower panel displays the measured depolarization factors for these samples. The reference lines indicate the point-by-point fit cutoff energies as displayed in Tab. I.

tion energies of $E_X = 2.21\,\text{eV}$, $E_\Gamma = 4.05\,\text{eV}$, $E_{X'} = 4.65\,\text{eV}$, and $E_{\Gamma'} = 5.45\,\text{eV}$. The large energy difference between the X' and Γ' transitions questions a previously assumed combined $\Gamma' X'$ transition[31]. For closer investigation, the transition dipole moments (TDMs) are calculated along the same high symmetry directions. For the X, Γ, X', and Γ' critical point transitions there are 3, 6, 2, and 5 bands involved of which 1, 3, 1, and 2 are conduction bands, respectively. Tab. II shows that the contributions from each valence band to the total TDM of a certain transition are equal independently on the number of conduction bands contributing to either transition. The total squared TDMs of X, Γ, X', and Γ' transitions, in units of $\text{e}^2\text{Å}^2$, amount to 14.0, 8.46, 0, and 11.6, respectively. We want to emphasize that the X' transition is symmetry forbidden (TDM $\equiv 0$), thus, what was labeled as combined $\Gamma' X'$ transition previously[31] is a Γ' transition only.

Table II: Total and valence band resolved squared transition dipole moments of rocksalt ScN for selected critical point transitions in units of $\text{e}^2\text{Å}^2$. Bands are labeled according to Fig. 1a

transition	transition dipole moment			
	total	VB 6	VB 7	VB 8
X	**14.0**	-	6.99	6.99
Γ	**8.46**	2.82	2.82	2.82
X'	**0**	0	-	-
Γ'	**11.6**	3.86	3.86	3.86

B. Spectroscopic ellipsometry

The data obtained from spectroscopic ellipsometry and corresponding point-by-point fit results are shown exemplary for samples A_1, C_1, and D in Fig. 2. The point-by-point fit matches the data nearly perfect for all AOIs above a certain energy, depending on the sample. This cutoff is the energy at which the measured depolarization factors (Fig. 2 lower panel) deviate for different AOIs, which coincides with the goodness of the point-by-point fit. The depolarization factors at different AOIs are mainly due to the appearance of incoherent interface reflections arising from the high film thicknesses[31]. Apart from sample D, the cutoff energy (Tab. I) increases with decreasing film thickness due to the low absorption by the indirect transitions in this spectral region. For sample D Fabry-Pérot fringes are observed, which are well modeled by our layer model and the point-by-point fit (see Fig. 2, right column). Here, for $E < 0.93\,\text{eV}$ the point-by-point fit does not describe the data adequately (see Fig. 2, right column), so for this sample the point-by-point cutoff is 0.93 eV. The depolarization factors of sample D deviate for $E < 2\,\text{eV}$, but they exhibit moderate values and oscillate consistently with the Fabry-Perot oscillations. This allows us to obtain the dielectric function of sample D down to 0.93 eV and hence direct evidence for the indirect bandgap in ScN from the imaginary part of the dielectric function (ε_2), although the sensitivity of ellipsometry to weak ε_2 for $\varepsilon_1 > 0$ is rather low. For sample A_1 the noise increases significantly at higher energies (see Fig. 2, left panel) due to the narrow slit width, which causes low signal-to-noise-ratio at the detector, and light diffraction at the surface roughness. For all samples the applied point-by-point fit results in excellent agreement with the data at photon energies larger than the above introduced cutoff energy.

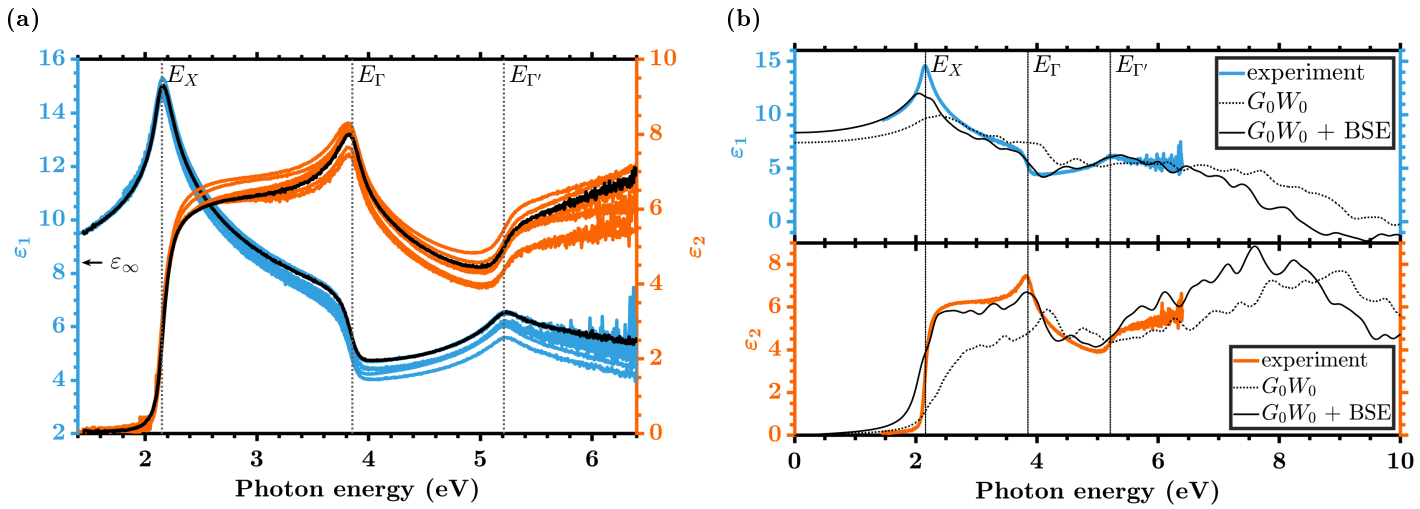

Figure 3: (a) Real (blue) and imaginary (orange) parts of the dielectric functions of all non-degenerate ScN samples determined from spectroscopic ellipsometry. The reference lines represent the averaged critical point transition energies. The black lines represent the dielectric function of sample A_1. (b) Comparison of experimental (sample A_2, blue/orange solid) and computed (G_0W_0: black dashed, G_0W_0 + BSE: black solid) real and imaginary parts of the dielectric function.

C. Dielectric function of ScN

The point-by-point fitted dielectric functions of all samples are displayed in Fig. 3a and show an excellent qualitative agreement. The quantitative deviation, which is stronger at higher energies, mainly stems from the treatment of the surface roughness, which is not sufficient for the purpose of quantitatively determining the absorption with high accuracy for the given surface structures. Below the absorption onset at $\approx 2.16\,\mathrm{eV}$, the real parts of the point-by-point fitted dielectric functions show a good agreement which strengthens the assumption of residual roughness effects at higher energies due to the low penetration depth of the incident light and increased diffraction and scattering effects for decreasing wave length. The imaginary part for sample A_1 (see Fig. 3a, black solid line) exhibits a lower amplitude above the absorption edge than previously published (e.g. 6.4 here and 7.3 in ref. [31] at 3 eV), which indicates, e.g., organic contamination on the surface which is now removed by the cleaning procedure in this work. This explains also the decrease of the roughness layer thickness from 8 nm[31] to 4.1 nm (see Tab. I).

Fig. 3b shows real and imaginary parts of the dielectric function of sample A_2, which exhibits the lowest free electron density, along with results from present theoretical calculations. The computational approach, including the solution of the Bethe-Salpeter-equation to account for electron-hole-interactions, shows an excellent even quantitative agreement with the experimental data, while the dielectric function calculated without solving the BSE deviates strongly in both amplitudes and transition energies. This behavior, which was observed before in e.g. AlN and CaO[44] or SnO_2[45], once again emphasizes the importance of electron-hole-interactions to be included in the computation of dielectric functions. The double peak structure at the X-point transition, i.e. the lowest direct band gap, is due to the overestimation of the exciton binding energy ($E_{bX} \approx 100\,\mathrm{meV}$). An estimate of (6-7)meV is obtained from the present calculations by taking into account the known convergence behavior of E_{bX} with the mesh size. As discussed below, this explains the absence of discrete excitons in ScN at room temperature. Additionally, the dielectric function determined from BSE shows some residual oscillations, where it was demonstrated in ref. [44] that such oscillations are due to a coarse k-point sampling. Calculations with coarser k-point sampling [46] reveal that, e.g., the Γ-point transition of ScN shows up as a clearly separable peak only if the mesh size is larger than $14 \times 14 \times 14$. Thus, a comparison of distinct features in the dielectric functions from theory and experiment is only valid if the mesh size is sufficiently large. The rather strong residual oscillations above 4.5 eV indicate that the present mesh size is not sufficiently large in this particular region. This is reasonable since the number of bands contributing to the dielectric response as well as off-symmetry point contributions increase with increasing photon energy.

To obtain the transition energies of critical point transitions from the experimental data we use the critical-point-parabolic-band (CPPB) model, where the n*th* derivative of $E^2\varepsilon$ is described by[47, 48]

$$\frac{d^n}{dE^n}(E^2\varepsilon) = \sum_j \frac{C_j e^{i\Phi_j}}{(E - E_j + i\Gamma_j)^{n+1}}. \qquad (3)$$

Here, C_j, Φ_j, E_j, and Γ_j are amplitude, phase, energy position, and broadening of the j*th* CP transition where we do not account for the dimensionality of each critical point. Although the model neglects excitons, the experimental data is described reasonably well and hence the energy positions of those transitions can be determined accurately, as discussed before[48]. Note, that eq. (3) is only applicable for $n \geq 2$ [48]. We use $n = 3$ for this work. The third derivatives of the dielectric functions are calculated using third order polynomial interpolation at each data point

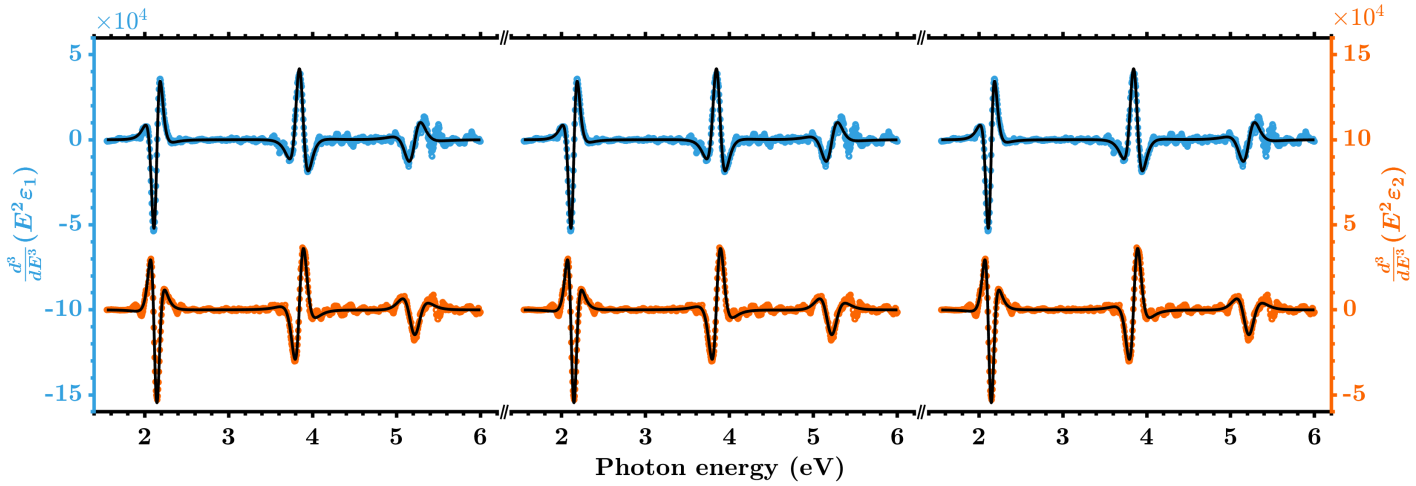

Figure 4: Exemplary results of the critical-point-parabolic-band (CPPB) model fitted to the third derivatives (real and imaginary part fitted simultaneously) of $E^2\varepsilon$ for samples A_2 (left panel), A_1 (middle panel), and D (right panel).

with dynamical interpolation widths [minimum 29 data points ($\hat{=}$0.14 eV) around 2.16 eV and maximum 81 data points ($\hat{=}$0.4 eV) above 5.6 eV]. Due to the better signal-to-noise-ratio, $\frac{d^3}{dE^3}(E^2\varepsilon) = E^2\frac{d^3\varepsilon}{dE^3} + 6E\frac{d^2\varepsilon}{dE^2} + 6\frac{d\varepsilon}{dE}$ was used to obtain $\frac{d^3}{dE^3}(E^2\varepsilon)$ from the first three derivatives of ε.

Eq. (3) was fitted simultaneously to the real and imaginary parts of $\frac{d^3}{dE^3}(E^2\varepsilon)$, which is exemplarily shown in Fig. 4 for samples A_1, A_2, and D, respectively. Only small deviations are visible around 2 eV in the spectra of all samples. We observe three distinct critical point transitions referred to E_X, E_Γ, and $E_{\Gamma'}$, located at around 2.16 eV, 3.85 eV, and 5.21 eV, respectively. The results look similar for all samples and the obtained fit parameters (see Supplement[46]) show high conformity across all samples. Because the residual strain is weak in our samples (see Tab. I), we choose to average the results of all samples to obtain a highly reliable value for the E_Γ and $E_{\Gamma'}$ transition energies. We determine $E_\Gamma = (3.853 \pm 0.006)$eV and $E_{\Gamma'} = (5.21 \pm 0.02)$eV where the error is given by the Student factor corrected (95% confidence interval) standard deviation. Theoretical calculations indicate that the energy shift due to residual strain is $\leq$ 2 meV (band gap deformation potential $\leq$ 2 eV [35]). The value for E_Γ is slightly higher than previously experimentally obtained 3.8 eV [8], where the deviation arises possibly from high strain in the thin films[8] and a different derivation technique. The low standard deviation of 6 meV indicates also that the bandgap renormalization does not affect the Γ-point, which is discussed in detail below. In contrast to the Γ-point transition, the X-point transition is expected to be influenced strongly by free electrons, which are located at the X-point. For comparison later on, we determine an averaged transition energy of $E_X^{(\mathrm{CPPB})} = (2.13 \pm 0.02)$eV. The third derivative of $(E^2\varepsilon)$ is very sensitive to detect barely separated or low magnitude transitions, so we have experimental evidence that the third critical point transition is not a combined X'/Γ' transition as we concluded before[31], unless they appear at the exact same energy ($\pm$0.05 eV). Because the present theoretical calculation predicts zero transition dipole matrix element for the X' transition, the third critical point transition can be assigned to $E_{\Gamma'}$ only.

For any M_0 type CP transition, the imaginary part of the dielectric function can be described by Elliott's model[49], which includes coulomb interactions between electron-hole-pairs. Assuming Gaussian broadening, the imaginary part of the dielectric function is given by

$$\varepsilon_2 = \frac{C}{E}\frac{1+\mathrm{erf}\left(\frac{E-E_X}{\gamma_X}\right)}{1-\exp\left(-2\pi\sqrt{\left|\frac{E_{\mathrm{bX}}}{E-E_X}\right|}\right)} + \varepsilon_{\mathrm{i}} \qquad (4)$$

where ε_{i} denotes the contribution of the indirect bandgap absorption, E_{bX} the exciton binding energy, and E_X the direct bandgap to be distinguished from the fundamental indirect bandgap E_{g}. In contrast to our recent work[31] we choose a more physically motivated model for the indirect bandgap absorption, following ref. 50:

$$\varepsilon_{\mathrm{i}} = \frac{C_{\mathrm{i}}}{E}\left[E - E_{\mathrm{g}}\right]^2 \Theta_{\mathrm{H}}(E - E_{\mathrm{g}}). \qquad (5)$$

Here, C_{i} is an arbitrary amplitude of the indirect bandgap absorption and Θ_{H} denotes the heaviside step-function. The C/E term in eqs. (4) and (5) is used instead of the nominal C/E^2 term to account for band non-parabolicity at energies above the respective transition. Discrete excitons are not included, as they are not observed[31]. The above-mentioned estimate for the exciton binding from the present calculation is $E_{\mathrm{bX}} \approx (6-7)$meV, while effective-mass-theory yields an even lower value ($E_{\mathrm{bX}} = \mu^*_{\mathrm{DOS}}/\varepsilon_{\mathrm{S}}^2 \times \mathrm{Ry} = 4$ meV) using effective masses and static dielectric constant from refs. [28] and [31], respectively. Thus, excitons are most likely thermally dissociated at room temperature and therefore not observed. Furthermore, a free electron density $> 10^{18}\,\mathrm{cm}^{-3}$ gives rise to significant screening of discrete excitons.

The dispersion of ε_1 can be described by Shokhovets' model[51], which can be further simplified for ScN. The dielectric function of the present theoretical calculation shows no prominent high energy contribution to ε_2 as it is the case

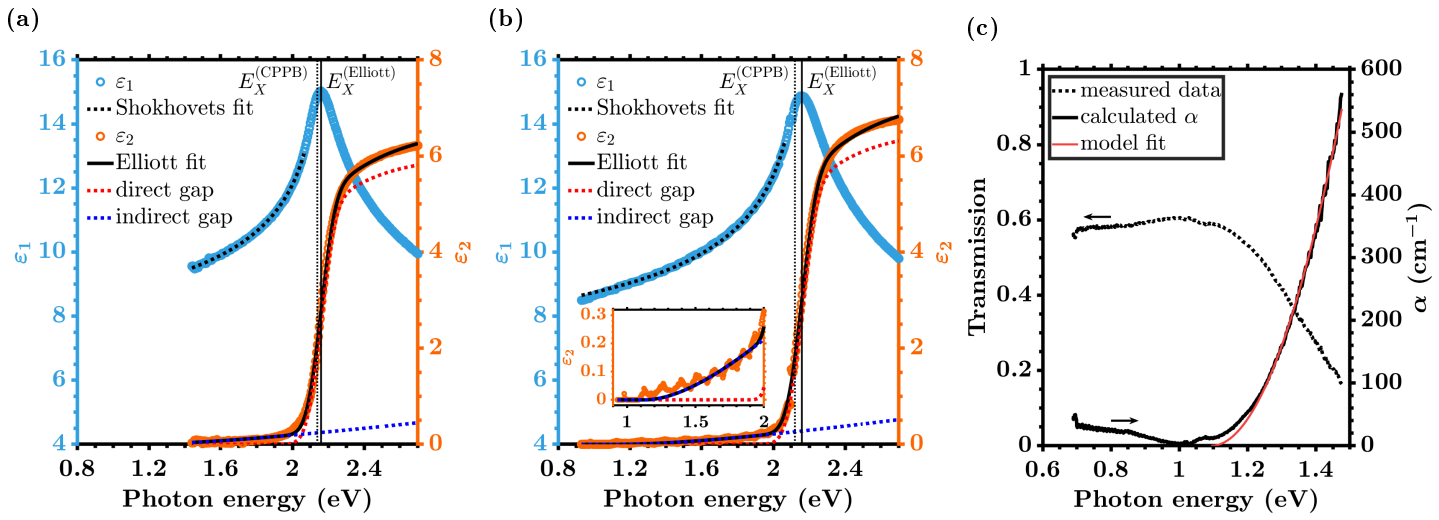

Figure 5: Exemplary results of modified Shokovets' and Elliott's model fitted to the real and imaginary parts of the point-by-point fitted dielectric function, respectively, of (a) sample A_1 and (b) sample D. The inset in (b) shows a close-up of the indirect absorption region. (c) Corrected normal incidence transmission (black dotted) and derived absorption coefficient α (black solid) for sample A_2. The model fit applied to the absorption coefficient is shown as well (red solid).

for e.g. AlN, GaN, and InN. So we choose to model the imaginary part of the dielectric function of ScN by

$$\varepsilon_2 = A_X \left[\Theta_H(E - E_X) - \Theta_H(E - E_h)\right] \tag{6}$$

which, after a Kramers-Kronig-transformation, yields

$$\varepsilon_1 = 1 + \frac{A_X}{\pi} \ln \left| \frac{E_h^2 - E^2}{E_X^2 - E^2} \right|. \tag{7}$$

If we treat the absorption edge E_X as a known value, this simplified version of Shokhovets' model has two free parameters. The dielectric limit of the electronic system, referred to as ε_∞, is given by $\varepsilon_\infty = \varepsilon_1(E \to 0)$.

Eqs. (4) and (7) are fitted to the imaginary and real parts of the point-by-point dielectric functions, respectively. For this purpose, the indirect bandgap E_g in eq. (5) is fixed at $1.08\,\text{eV} + \Delta E_{BMS}$ (see supplement for the equation of ΔE_{BMS}) and the upper limit of the fit range is set to 2.7 eV to exclude residual absorption contributions from higher energy transitions within the Elliott model fit. When applying eq. (7) to the real part of the dielectric function, E_X was fixed to the value obtained by Elliotts' model and the upper limit of the fit range is set to $E_X - \gamma_X$. Fit results are displayed in Figs. 5a and 5b exemplarily for samples A_1 and D, respectively. We find an excellent agreement between data and fit for the real part of the dielectric function for all samples except of sample D. Because sample D exhibits the highest free electron concentration, we add a Drude contribution with fixed plasma-frequency, as derived from the given carrier density and $m^*_{e,DOS} = 0.35 m_e$, yielding an ε_∞ very close to the other samples. Note, that the line shape is still not described adequately and that the resulting plasma broadening is $\gamma_P = 5\,\text{meV}$ ($25\,\text{cm}^{-1}$). The determined values for ε_∞ exhibit high conformity, where only sample C_1 is an outlier (see Tab I. of supplement [46]). Nevertheless, the fit describes the data excellently for low doped samples. Because ε_1 is very similar for all samples below the direct bandgap (see Fig. 3a), results of sample A_2 (second lowest free carrier density and lowest pbp cutoff energy) are taken as an estimate for intrinsic ScN. We have $\varepsilon_\infty = 8.38 \pm 0.04$, which is slightly higher than in our previous work[31], but well within the given uncertainty. The dielectric limit derived from the BSE dielectric function is $\varepsilon_\infty = 8.33$ which perfectly matches the experimental value.

Applying eqs. (4) and (5) to the imaginary parts of the dielectric functions results in a good agreement between data and model (see Figs. 5a and 5b for samples A_1 and D exemplarily). The inset of Fig. 5b demonstrates that the indirect band gap model with the assumed $E_g = 1.08\,\text{eV} + \Delta E_{BMS}$ describes the weak absorption reasonably for sample D, which, in contrast to all other samples, has a pbp cutoff energy below its bandgap. The lowest direct absorption edge energies E_X, as determined from Elliott's model, are in a narrow range from 2.150 eV to 2.160 eV. Given the experimental spectral resolution of 4 meV at 2.2 eV, we can conclude that the absorption edges do not shift significantly over the entire carrier density range ($1.3 \times 10^{18}\,\text{cm}^{-3}$ to $2.7 \times 10^{19}\,\text{cm}^{-3}$). In average we have (2.156±0.007)eV, which is a slightly higher value than determined from the CPPB model: $E_X^{(CPPB)} = (2.13 \pm 0.02)$eV. This is not surprising, since the CPPB model does not include excitons and hence one determines the sharp onset of absorption rather than the true absorption edge which is located near the inflection point of ε_2 (see vertical lines in Figs. 5a and 5b). The broadenings range from 72 meV to 91 meV, which is well above room temperature $k_B T$, indicating additional broadening mechanisms. The exciton binding energies derived from Elliott's model scatter from 14.2 meV to 21.5 meV, which demonstrates that this fit parameter is very sensitive to the underlying indirect bandgap absorption strength, although no clear trend of the indirect absorption strength with respect to the exciton binding energy is observed (see Tab. I. of supplement[46]). This is

reasonable, since in the absence of discrete exciton states the exciton binding energy only determines the strength of the Sommerfeld enhancement factor [denominator in eq. (4)], which of course overlaps with any other residual absorption above the absorption edge. The average exciton binding energy is $E_{\mathrm{bX}} = (17 \pm 5)$meV in good agreement with our previous work[31], but about three times the value estimated from effective-mass-theory and the present theoretical calculations. Thus, the exciton binding energy can not be determined unambiguously in this work.

To determine the indirect band gap, normal incidence transmission is measured on sample B_2. The absorption-coefficient α is obtained by

$$T = (1 - \sum_{j=1}^{N} R_j) \exp\{-\alpha d\} \tag{8}$$

where d denotes the sample thickness and R_j the reflection losses at the jth interface. Losses due to multiple interface reflections are omitted in eq (8), which is a reasonable approximation given the large thicknesses of ScN film and sapphire substrate. Reflection losses are included for air/ScN, ScN/sapphire, and sapphire/air interfaces, i.e. $N = 3$. Therefore, the model dispersion curves of ε_1, i.e. the Shokhovets' model fit results for ScN and an average of ordinary and extraordinary component from ref. [52] for sapphire, are used to calculate the respective interface reflections via $R_j = (\sqrt{\varepsilon_{1,j-1}} - \sqrt{\varepsilon_{1,j}})^2/(\sqrt{\varepsilon_{1,j-1}} + \sqrt{\varepsilon_{1,j}})^2$, where $j = 0, 3$ correspond to the front and backside ambient air, respectively. The resulting absorption coefficient is slightly negative, which is likely due to a slight misalignment of probe and reference light hole sizes. Thus, the measured transmission is multiplied by a factor of 0.93 to ensure that α is positive at all wave lengths. The resulting data and thereof calculated absorption coefficient are displayed in Fig. 5c. The onset of absorption due to the indirect band gap around 1.1 eV is clearly visible. To derive an estimate for the indirect band gap, the derived α is fitted using $\alpha = \omega\varepsilon_2/c\sqrt{\varepsilon}$ and eqs. (7) and (5) for ε_1 and ε_2, respectively, where the parameters for ε_1 are set to the values obtained from fitting the pbp ε_1 of sample B_2. Fit results are also shown in Fig. 5c (red line), where a good agreement between fit and data is found for $E > 1.2$ eV. Because the model does not account for broadening, the lower limit of the fit range is set to 1.22 eV, which is obtained by a maximization of the adjusted coefficient of determination $\tilde{r}$ upon varying lower fit range limit. The obtained band gap is $E_{\mathrm{g}} = (1.09 \pm 0.02)$eV, where the uncertainty is estimated from the variation of E_{g} upon varying lower fit range limit.

To derive estimates for true intrinsic direct and indirect bandgap, we have to account for many-body effects on the absorption edge. Free carriers shift both, the bandgap and the absorption edge by means of bandgap renormalization (BGR) and band-filling, known as Burstein-Moss-shift (BMS), respectively. The parabolic band approximation is near-exact in the non-degenerate regime and the functional dependence of a transition energy E_{CV} on the free carrier density reads qualitatively

$$E_{\mathrm{CV}}(n) = E_{\mathrm{CV},0} + \Delta E_{\mathrm{BGR}}(n,\ m^*_{\mathrm{e/h,DOS}},\ \varepsilon_{\mathrm{S}},\ \nu) + \Delta E_{\mathrm{BMS}}(n,\ m^*_{\mathrm{e,DOS}},\ \nu). \tag{9}$$

Here, ν is the manifold of the conduction band minimum and ε_{S} the low frequency dielectric constant. Note that we assume the valence band contribution to the BMS to be negligible in the non-degenerate regime. Using the effective valence and conduction band masses from Ref. 28 and $\varepsilon_{\mathrm{S}} = 29.5$ from Ref. 31, $E_{\mathrm{CV},0}$ is the only free parameter remaining in eq. 9. The explicit equations for the BGR, as derived in ref. [53], and the BMS as well as values for the effective masses are given in the supplement[46].

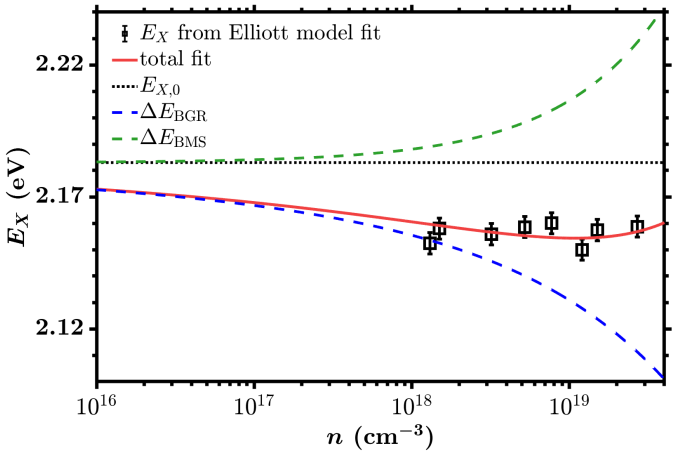

Figure 6: Direct absorption edge E_X as determined from Elliotts' model (black squares) plotted against the free carrier concentration n along with model fit results (red solid) and respective contributions (bandgap renormalization: blue dashed, Burstein-Moss-Shift: green dashed).

Fig. 6 displays the applied fit of eq. (9) to $E_X^{(\mathrm{Elliott})}$ over n, where n is the free electron concentration determined from Hall measurements. We obtain a slight decrease of E_X with increasing n due to the BGR before the BMS shifts the absorption edge to higher energies again. The assumed effective masses and ε_{S} reflect the near constant absorption edges of our samples from $1.3 \times 10^{18}\,\mathrm{cm}^{-3}$ to $2.7 \times 10^{19}\,\mathrm{cm}^{-3}$ reasonably, where the scattering around the fit curve may arises from e.g. small residual strain effect and fitting errors. The fit yields an intrinsic direct bandgap of $E_{X,0} = (2.182 \pm 0.004)$eV, which is close to an earlier reported absorption edge of non-degenerate ScN ($E_X = 2.15$ eV[54]), but deviates from previously published values extrapolated from degenerately doped films (2.1 eV[7] and (2.07±0.05)eV[8]). This is because the BGR was not taken into account in these works. The present band structure calculations yield $E_X = 2.21$ eV, hence less than 1.5 % deviation from the experimental value. Note, that in ref. [42] almost the same transition energy was obtained from an extended *QSGW* scheme, where the electron-phonon interaction renormalization was also considered[42]. They obtained a corrected X-point gap of 2.23 eV, which deviates less than 2.5 % from the present experimental value. Thus, the renormalization of

Table III: Comparison of intrinsic indirect and direct band gaps, higher energy critical point transition energies, and the dielectric constant determined in this work and from selected theoretical works..

	E_g (eV)	E_X (eV)	E_Γ (eV)	$E_{\Gamma'}$ (eV)	ε_∞
experiment (this work)	**1.08(2)**	**2.182(4)**	**3.853(6)**	**5.21(2)**	**8.38(4)**
theory (this work, G_0W_0)	**1.09**	**2.21**	**4.05**	**5.45**	**8.33 [BSE]**
theory (OEPx[cLDA]-G_0W_0) [35]	0.84	1.98	3.51	4.72	-
theory (LDA-G_0W_0) [35]	1.14	2.06	3.71	-	-
theory (HSE25 with 25% quasiparticle mix) [28]	0.79	1.91	3.58	4.74	9.8
theory (HSE06 with hybrid exchange correlation potential) [8]	0.92	2.02	3.72	4.9	7.6

the exciton continuum transition energy at the X-point due to electron-hole-pair interactions is of low magnitude. The remaining deviation between theory and experiment is reasonable since measurements are performed at room temperature while the present computations yield the band structure and dielectric function at $T = 0\,\mathrm{K}$.

We now include experimental results by angular-resolved photoelectron-spectroscopy (ARPES) of degenerately doped, bulk ScN into our discussion[6]. We can conduct further conclusions regarding the bandgap renormalization in ScN from the following assessments: The expected bandgap shrinkage due to BGR amounts to 28 meV at $1 \times 10^{18}\,\mathrm{cm}^{-3}$ and 74 meV at $3 \times 10^{19}\,\mathrm{cm}^{-3}$, while no shrinkage of the E_Γ and $E_{\Gamma'}$ transition energies between those carrier densities is found. Additionally, this transition is almost perfectly resembled by the present theory. Hence, as $\Gamma-$point transitions do not underlie the BMS to compensate the BGR, we may conclude that the BGR does not affect any transitions located near the Γ-point. Ref. 6 consistently reports a BMS of $\approx 370\,\mathrm{meV}$ and a BGR of $\approx -340\,\mathrm{meV}$ at the X-point while the indirect bandgap ($\overline{\Gamma X}$) is 1.2 eV, so we further conclude that the bandgap renormalization in ScN affects only the local environment in reciprocal space of the valence band at the X-point and does not affect the conduction band at all. This is clearly visible by the formation of a local valence band maximum in their experimentally determined electronic band structure (see Fig. 2c in Ref. 6). This implies that the indirect bandgap, as determined from transmission measurements on sample B_2, is affected by the BMS only, yielding an intrinsic indirect bandgap of $E_{g,0} = (1.08 \pm 0.02)\mathrm{eV}$, which is only slightly lower than that in Ref. 6 (1.2 eV).

In summary, we derived highly reliable electronic transition energies from non-degenerately doped quasi-bulk ScN single crystals as listed in Tab. III and presented a detailed comparison with state-of-the-art computations. Intrinsic direct and indirect bandgaps are extrapolated with an approximate accuracy $\leq 20\,\mathrm{meV}$ from experiment by taking into account free carrier effects. The E_Γ and $E_{\Gamma'}$ critical point transition energies are derived in a statistical manner with uncertainties of 6 meV and 20 meV, respectively, from experiment. We find further evidence that the bandgap renormalization does not affect the band structure near the Γ-point in ScN. The present theory shows exceptional agreement of the direct X and Γ-point transition energies as well as the dielectric limit of the electronic system if electron-hole-interaction, i.e. the Bethe-Salpeter-equation, are considered. Additionally we demonstrated that the X'-transition is symmetry forbidden and therefore not observed in experiment, while the Γ'-transition energies derived from theory and experiment align. The critical point transition energies obtained from the G_0W_0 band structure, i.e. in the omission of electron-hole-interactions, show almost linearly increasing deviation from the experimental values for increasing energies (see Tab. III). Hence, this work once again demonstrates the importance of electron-hole-interactions to be included to derive the optical response of semiconductors properly. This is true even in the absence of discrete exciton states as it is the case here. The exciton binding energy has yet to be determined precisely in ScN since the present approaches only yield estimates.

This work was partially funded by the *Deutsche Forschungsgemeinschaft* within the framework of the priority programme 2312 (GaNius) under grant No. 462722619 and contract FE1453/2-1. H.A. would like to thank Prince Sultan University for their support in providing computational resources. We acknowledge Duc V. Dinh from *Paul-Drude-Institut für Festkörperelektronik* (Berlin, Germany) for conducting the Hall measurements on the present samples. We also acknowledge our in-house partner Jürgen Bläsing for the determination of lattice parameters. We thank Daniel Gall and and Sai Mu for providing the theoretical data of Refs. 8 and 28, respectively.

[1] Z. Gu, J. H. Edgar, J. Pomeroy, M. Kuball, and D. W. Coffey, Crystal growth and properties of scandium nitride, J. Mater. Sci.: Mater. Electron. **15**, 555 (2004).
[2] R. Niewa, D. A. Zherebtsov, M. Kirchner, M. Schmidt, and W. Schnelle, New Ways to High-Quality Bulk Scandium Nitride, Chem. Mater. **16**, 5445 (2004).
[3] Y. Oshima, E. G. Víllora, and K. Shimamura, Hydride vapor phase epitaxy and characterization of high-quality ScN epilayers, J. Appl. Phys. **115**, 153508 (2014).
[4] H. A. Al-Atabi, N. Khan, E. Nour, J. Mondoux, Y. Zhang,

and J. H. Edgar, Bulk (100) scandium nitride crystal growth by sublimation on tungsten single crystal seeds, Appl. Phys. Lett. **113**, 122106 (2018).
[5] H. A. Al-Atabi, Q. Zheng, J. S. Cetnar, D. Look, D. G. Cahill, and J. H. Edgar, Properties of bulk scandium nitride crystals grown by physical vapor transport, Appl. Phys. Lett. **116**, 132103 (2020).
[6] H. A. Al-Atabi, X. Zhang, S. He, C. Chen, Y. Chen, E. Rotenberg, and J. H. Edgar, Lattice and electronic structure of ScN observed by angle-resolved photoemission spectroscopy measurements, Appl. Phys. Lett. **121**, 182102 (2022).
[7] J. Dismukes, W. Yim, and V. Ban, Epitaxial growth and properties of semiconducting ScN, J. Cryst. Growth **13-14**, 365 (1972).
[8] R. Deng, B. D. Ozsdolay, P. Y. Zheng, S. V. Khare, and D. Gall, Optical and transport measurement and first-principles determination of the ScN band gap, Phys. Rev. B **91**, 045104 (2015).
[9] M. A. Moram, Y. Zhang, M. J. Kappers, Z. H. Barber, and C. J. Humphreys, Dislocation reduction in gallium nitride films using scandium nitride interlayers, Appl. Phys. Lett. **91**, 152101 (2007).
[10] S. Kerdsongpanya, N. van Nong, N. Pryds, A. Žukauskaitė, J. Jensen, J. Birch, J. Lu, L. Hultman, G. Wingqvist, and P. Eklund, Anomalously high thermoelectric power factor in epitaxial ScN thin films, Appl. Phys. Lett. **99**, 232113 (2011).
[11] D. Rao, B. Biswas, E. Flores, A. Chatterjee, M. Garbrecht, Y. R. Koh, V. Bhatia, A. I. K. Pillai, P. E. Hopkins, M. Martin-Gonzalez, and B. Saha, High mobility and high thermoelectric power factor in epitaxial ScN thin films deposited with plasma-assisted molecular beam epitaxy, Appl. Phys. Lett. **116**, 152103 (2020).
[12] M. Akiyama, K. Kano, and A. Teshigahara, Influence of growth temperature and scandium concentration on piezoelectric response of scandium aluminum nitride alloy thin films, Appl. Phys. Lett. **95**, 162107 (2009).
[13] S. Fichtner, N. Wolff, F. Lofink, L. Kienle, and B. Wagner, AlScN: A III-V semiconductor based ferroelectric, J. Appl. Phys. **125**, 114103 (2019).
[14] J. Klein, L. Kampermann, B. Mockenhaupt, M. Behrens, J. Strunk, and G. Bacher, Limitations of the Tauc Plot Method, Adv. Funct. Mater. **33**, 2304523 (2023).
[15] P. E. Blöchl, Projector augmented-wave method, Phys. Rev. B **50**, 17953 (1994).
[16] G. Kresse and D. Joubert, From ultrasoft pseudopotentials to the projector augmented-wave method, Phys. Rev. B **59**, 1758 (1999).
[17] G. Kresse and J. Furthmüller, Efficient iterative schemes for ab initio total-energy calculations using a plane-wave basis set, Phys. Rev. B **54**, 11169 (1996).
[18] J. Heyd, G. E. Scuseria, and M. Ernzerhof, Hybrid functionals based on a screened Coulomb potential, J. Chem. Phys. **118**, 8207 (2003).
[19] J. Heyd and G. E. Scuseria, Efficient hybrid density functional calculations in solids: Assessment of the Heyd-Scuseria-Ernzerhof screened Coulomb hybrid functional, J. Chem. Phys. **121**, 1187 (2004).
[20] J. P. Perdew, K. Burke, and M. Ernzerhof, Generalized Gradient Approximation Made Simple, Phys. Rev. Lett. **77**, 3865 (1996).
[21] H. J. Monkhorst and J. D. Pack, Special points for brillouin-zone integrations, Phys. Rev. B **13**, 5188 (1976).
[22] G. Pizzi, V. Vitale, R. Arita, S. Blügel, F. Freimuth, G. Géranton, M. Gibertini, D. Gresch, C. Johnson, T. Koretsune, J. Ibañez-Azpiroz, H. Lee, J.-M. Lihm, D. Marchand, A. Marrazzo, Y. Mokrousov, J. I. Mustafa, Y. Nohara, Y. Nomura, L. Paulatto, S. Poncé, T. Ponweiser, J. Qiao, F. Thöle, S. S. Tsirkin, M. Wierzbowska, N. Marzari, D. Vanderbilt, I. Souza, A. A. Mostofi, and J. R. Yates, Wannier90 as a community code: new features and applications, J. Phys.: Condens. Matter **32**, 165902 (2020).
[23] R. Deng, B. D. Ozsdolay, P. Y. Zheng, S. V. Khare, and D. Gall, Optical and transport measurement and first-principles determination of the ScN band gap, Phys. Rev. B **91**, 045104 (2015).
[24] A. Schleife, C. Rödl, F. Fuchs, J. Furthmüller, and F. Bechstedt, Optical and energy-loss spectra of MgO, ZnO, and CdO from ab initio many-body calculations, Phys. Rev. B - Condens. Matter Mater. Phys. **80**, 1 (2009).
[25] A. Schleife and F. Bechstedt, Ab initio description of quasiparticle band structures and optical near-edge absorption of transparent conducting oxides, J. Mater. Res. **27**, 2180 (2012).
[26] M. Rohlfing and S. G. Louie, Electron-hole excitations and optical spectra from first principles, Phys. Rev. B **62**, 4927 (2000).
[27] D. A. G. Bruggeman, Berechnung verschiedener physikalischer Konstanten von heterogenen Substanzen. I. Dielektrizitätskonstanten und Leitfähigkeiten der Mischkörper aus isotropen Substanzen, Ann. Phys. **416**, 636 (1935).
[28] S. Mu, A. J. E. Rowberg, J. Leveillee, F. Giustino, and C. G. van de Walle, First-principles study of electron transport in ScN, Phys. Rev. B **104**, 075118 (2021).
[29] Y. Kumagai, N. Tsunoda, and F. Oba, Point Defects and p -Type Doping in ScN from First Principles, Phys. Rev. Appl. **9**, 034019 (2018).
[30] M. A. Moram, Z. H. Barber, C. J. Humphreys, T. B. Joyce, and P. R. Chalker, Young's modulus, Poisson's ratio, and residual stress and strain in (111)-oriented scandium nitride thin films on silicon, J. Appl. Phys. **100**, 023514 (2006).
[31] J. Grümbel, R. Goldhahn, M. Feneberg, Y. Oshima, A. Dubroka, and M. Ramsteiner, Band gaps and phonons of quasi-bulk rocksalt ScN, Phys. Rev. Mater. **8**, L071601 (2024).
[32] P. Weinberger, K. Schwarz, and A. Neckel, Electronic band structure of ScN, J. Phys. Chem. Solids **32**, 2063 (1971).
[33] W. R. L. Lambrecht, Electronic structure and optical spectra of the semimetal ScAs and of the indirect-band-gap semiconductors ScN and GdN, Phys. Rev. B **62**, 13538 (2000).
[34] D. Gall, M. Städele, K. Järrendahl, I. Petrov, P. Desjardins, R. T. Haasch, T.-Y. Lee, and J. E. Greene, Electronic structure of ScN determined using optical spectroscopy, photoemission, and ab initio calculations, Phys. Rev. B **63**, 125119 (2001).
[35] A. Qteish, P. Rinke, M. Scheffler, and J. Neugebauer, Exact-exchange-based quasiparticle energy calculations for the band gap, effective masses, and deformation potentials of ScN, Phys. Rev. B **74**, 245208 (2006).
[36] L. Tie-Yu and H. Mei-Chun, Electronic structure of ScN and YN: density-functional theory LDA and *GW* approximation calculations, Chinese Phys. **16**, 62 (2007).
[37] W. Xue, Y. Yu, Y. Zhao, H. Han, and T. Gao, First principles calculations of the electronic, dynamical, and thermodynamic properties of the rocksalt ScX (X=N, P, As, Sb), Computational Materials Science **45**, 1025 (2009).
[38] B. Saha, J. Acharya, T. D. Sands, and U. V. Waghmare, Electronic structure, phonons, and thermal properties of ScN, ZrN, and HfN: A first-principles study, J. Appl. Phys. **107**, 033715 (2010).
[39] B. Ul Haq, A. Afaq, G. Abdellatif, R. Ahmed, S. Naseem, and R. Khenata, First principles study of scandium nitride and yttrium nitride alloy system: Prospective material for optoelectronics, Superlattices and Microstructures **85**, 24 (2015).
[40] A. S. Botana, V. Pardo, and W. E. Pickett, Nitride multilayers as a platform for parallel two-dimensional electron-hole gases: Mgo/scn(111), Phys. Rev. B **93**, 085125 (2016).
[41] J. M. Waack, M. Kremer, M. Czerner, and C. Heiliger, Struc-

tural and electronic properties of cubic rocksalt $Al_xSc_{1-x}N$ random alloys from ab initio calculations, Phys. Rev. B **109**, 075142 (2024).

[42] B. Cunningham, M. Grüning, D. Pashov, and M. van Schilfgaarde, $QSG\hat{W}$: Quasiparticle self-consistent GW with ladder diagrams in W, Phys. Rev. B **108**, 165104 (2023).

[43] M. Großmann, M. Thieme, M. Grunert, and E. Runge, Many-body perturbation theory vs. density functional theory: A systematic benchmark for band gaps of solids (2025), arXiv:2508.05247 [cond-mat.mtrl-sci].

[44] A. Riefer, F. Fuchs, C. Rödl, A. Schleife, F. Bechstedt, and R. Goldhahn, Interplay of excitonic effects and van hove singularities in optical spectra: CaO and AlN polymorphs, Phys. Rev. B **84**, 075218 (2011).

[45] M. Feneberg, C. Lidig, K. Lange, R. Goldhahn, M. D. Neumann, N. Esser, O. Bierwagen, M. E. White, M. Y. Tsai, and J. S. Speck, Ordinary and extraordinary dielectric functions of rutile sno_2 up to 20 ev, Appl. Phys. Lett. **104**, 231106 (2014).

[46] See Supplemental Material at [] for (i) bandgap renormalization and Burstein-Moss-Shift equations, (ii) a list of fit parameters for all samples, and (iii) the computed dielectric function up to 60 eV and that for different mesh sizes.

[47] D. E. Aspnes, Third-derivative modulation spectroscopy with low-field electroreflectance, Surf. Sci. **37**, 418 (1973).

[48] C. C. Kim, J. W. Garland, H. Abad, and P. M. Raccah, Modeling the optical dielectric function of semiconductors: Extension of the critical-point parabolic-band approximation, Phys. Rev. B **45**, 11749 (1992).

[49] R. J. Elliott, Intensity of Optical Absorption by Excitons, Phys. Rev. **108**, 1384 (1957).

[50] M. Feneberg, J. Nixdorf, C. Lidig, R. Goldhahn, Z. Galazka, O. Bierwagen, and J. S. Speck, Many-electron effects on the dielectric function of cubic In_2O_3 : Effective electron mass, band nonparabolicity, band gap renormalization, and Burstein-Moss shift, Phys. Rev. B **93**, 045203 (2016).

[51] S. Shokhovets, R. Goldhahn, G. Gobsch, S. Piekh, R. Lantier, A. Rizzi, V. Lebedev, and W. Richter, Determination of the anisotropic dielectric function for wurtzite AlN and GaN by spectroscopic ellipsometry, J. Appl. Phys. **94**, 307 (2003).

[52] I. H. Malitson and M. J. Dodge, Refractive index and birefringence of synthetic sapphire, J. Opt. Soc. Am **62**, 1405 (1972).

[53] K.-F. Berggren and B. E. Sernelius, Band-gap narrowing in heavily doped many-valley semiconductors, Phys. Rev. B **24**, 1971 (1981).

[54] H. A. Al-Brithen, A. R. Smith, and D. Gall, Surface and bulk electronic structure of ScN(001) investigated by scanning tunneling microscopy/spectroscopy and optical absorption spectroscopy, Phys. Rev. B **70**, 045303 (2004).